Available online at www.sciencedirect.com
SCIENCE DIRECT
Journal of Photochemistry and Photobiology A: Chemistry 176 (2005) 208–217
Journal of Photochemistry and Photobiology A:Chemistry
www.elsevier.com/locate/jphotochem

T-dependent rate measurements of homogeneous ice nucleation in cloud droplets using a large atmospheric simulation chamber

Stefan Benz, Khaled Megahed, Ottmar Möhler, Harald Saathoff, Robert Wagner, Ulrich Schurath *

Forschungszentrum Karlsruhe, Institute for Meteorology and Climate Research (IMK-AAF), PO Box 3640, D-76021 Karlsruhe, Germany

Available online 19 September 2005

Abstract

The rates of photochemical reactions in the atmosphere depend on the optical properties and lifetimes of clouds. These are critically affected by the process of droplet freezing, because ice crystals can grow to large sizes at the expense of the metastable supercooled droplets, thereby initiating graupel formation and precipitation. The large evacuable and coolable aerosol chamber AIDA at Forschungszentrum Karlsruhe has been used to generate supercooled clouds under controlled conditions. Homogeneous freezing was detected below −35.5 °C, and nucleation rates $J(T)$ were measured to about −37 °C. They vary between $\sim 10^6$ cm^{-3} s^{-1} at the highest and $\sim 10^8$ cm^{-3} s^{-1} at the lowest temperature, although the temperature dependence of the nucleation rate is not very well constrained by the measurements. The results agree within the combined error limits with recent literature data. Homogeneous ice nucleation, which sets a lower limit to cloud freezing temperatures when other nucleation mechanisms are inefficient in the atmosphere, is important in deep convective systems and in cirrus.

Keywords: Cloud chamber; Droplet freezing; Nucleation rate

1. Introduction

The lifetimes of trace gases in the atmosphere depend either directly or indirectly (via removal by OH radicals) on photochemistry [1]. Aerosol particles affect the rates of photochemical reactions in the atmosphere directly by scattering and absorption of solar radiation [2]. Significantly stronger is the effect of changing cloudiness on photochemical rates [3,4]. The attenuation of solar radiation by clouds depends on their lifetimes which decrease when supercooled clouds glaciate, because ice particles grow rapidly at the expense of the supercooled cloud droplets due to a significant difference in vapour pressures (Bergeron–Findeisen process [5]). This initiates rainfall from otherwise non-precipitating clouds. While glaciation at temperatures above about −35 °C can only be triggered by seeding a cloud with ice particles from above, or by heterogeneous ice nucleation which can be triggered within the cloud by a small sub-set of aerosol particles (so-called ice nuclei) via a number of different mechanisms [6], homogeneous freezing of cloud droplets is dominant in deep convective systems with strong updrafts and concomitantly high cooling rates and in cirrus [7–9].

Classical nucleation theory and its application to homogeneous freezing of supercooled water clouds have been reviewed by Pruppacher [10], and more recently by Koop [11]. Pruppacher's parameterisation of the ice nucleation rate in supercooled water has been modified by Huang and Bartell [12] and by Jeffery and Austin [13] to include experimental data over a wider temperature range. In spite of its fundamental importance in convective systems [14], homogeneous ice nucleation rates of supercooled droplets are hard to determine accurately and with good precision, making it very difficult to test nucleation theories. Molecular dynamics simulations, although computationally extremely demanding when applied to the strongly hydrogen-bonded water system [15], have fostered our understanding of the homogeneous freezing process while shedding some doubt on the validity of classical nucleation theory. For example, the

* Corresponding author. Tel.: +49 7247 82 2659; fax: +49 7247 82 4332.
E-mail addresses: Stefan.Benz@imk.fzk.de (S. Benz), Khaled.Megahed@imk.fzk.de (K. Megahed), Ottmar.Moehler@imk.fzk.de (O. Möhler), Harald.Saathoff@imk.fzk.de (H. Saathoff), Robert.Wagner@imk.fzk.de (R. Wagner), Ulrich.Schurath@imk.fzk.de (U. Schurath).

1010-6030/$ – see front matter © 2005 Elsevier B.V. All rights reserved.
doi:10.1016/j.jphotochem.2005.08.026

validity of bulk properties like surface tension to evaluate the energetics of the critical nucleus is highly questionable.

Until recently it has been generally accepted that the probability of homogeneous ice nucleation is proportional to the volume, i.e. to the third power of the diameter of the supercooled droplet which freezes. However, Tabazadeh et al. argue that ice nucleation occurs preferentially at the air–water interface, at least for very small droplets with large surface/volume ratios, thereby yielding a freezing probability proportional to the diameter squared [16]. Evidence in support of this assumption comes from molecular dynamics simulations of extremely small supercooled SeF_6 droplets which were found to nucleate preferentially at or near the droplet surface [17]. However, recent homogeneous freezing experiments with pure water droplets of much larger sizes which were levitated in a Paul trap clearly indicate that the freezing rate scales with the third power of the droplet diameter, at least for droplets larger than 8 μm, and most likely also for smaller ones [18]. Evidence in favour of either surface or volume induced ice nucleation in airborne water drops has also been discussed by Koop in his recent review [11].

Here we report homogeneous nucleation rates $J(T)$, based on three experiments in artificial supercooled water clouds which were generated and cooled below the homogeneous freezing threshold of about −35.5 °C by slow expansions of a humid sulphuric acid aerosol in a large evacuable simulation chamber. Cooling rates were not constant due to the isothermal chamber walls – in contrast to an earlier cloud chamber study by DeMott and Rogers who used a temperature programmed cold shield to simulate adiabatic expansion cooling [19] – but varied between 5 K min^{-1} and less than 0.2 K min^{-1}. This corresponds to vertical velocities between 8 and 0.3 m s^{-1} in clear air. The results are critically evaluated and compared with other experimental data and recommended parameterisations of the nucleation rate.

2. Experimental

Experiments were carried out in the large aerosol chamber AIDA ("Aerosol Interactions and Dynamics in the Atmosphere") of Forschungszentrum Karlsruhe [20]. It is a cylindrical aluminium vessel, wall thickness 20 mm, inner diameter 4 m, volume 84 m^3, which can be evacuated to ca. 1 Pa with two large mechanical pumps. The vessel is mounted vertically in a large containment which isolates the chamber from the surrounding laboratory platforms, as shown schematically in Fig. 1. It can be operated by evaporating either a refrigerant from a chiller to access temperatures in the range +40 to −35 °C, or liquid nitrogen from a tank lorry when temperatures in the range −35 to −90 °C are required. Different heat exchangers are used for these refrigerants. The air in the containment is forced through the heat exchangers by powerful blowers and circulates around the aluminium vessel to homogenise the temperature of the chamber walls. The air inside the aluminium vessel is continuously mixed with a ventilator. Deviations from the mean air temperature which is routinely monitored with nine calibrated sensors (Fig. 1) rarely exceed ±0.3 °C during experiments.

The following instruments are relevant for the experiments described below: water vapour is measured in situ with a time resolution of 1 s using a tuneable DFB (distributed feedback) diode laser which scans across a suitable rovibrational line of an overtone transition in the wavelength regime 1368–1371 nm, as described in detail elsewhere [21]. The sensitivity is enhanced by a White mirror arrangement which provides an optical path length of 82 m inside the chamber. The estimated uncertainty of the TDL system is ±5%. Note that the system is only sensitive to interstitial water vapour. Water in condensed phases is measured simultaneously with an FTIR spectrometer (Bruker, IFS 66v) in combination with another White mirror arrangement which provides optical path lengths up to 254.3 m in the chamber. Extinction spectra in the range 800–6000 cm^{-1} were recorded once every 10 s and analysed using Mie theory with recently determined complex refractive indices of supercooled water [22] to retrieve the volume densities and droplet diameters in the chamber, and to identify the ice phase when formed. Total water is measured ex situ with a high precision frost point hygrometer (MBW, model 373, option LX) which is connected with the chamber via a heated sampling tube to evaporate droplets and small ice crystals. Aerosol number concentrations and size distributions are measured with a condensation particle counter (TSI CNC 3010) and a low temperature differential mobility particle sizer (DMPS) [23], while size distributions of cloud droplets are measured with a time resolution of 3 s with an optical particle counter (WELAS, Palas GmbH) which was operated under chamber conditions (cf. Fig. 1) at a flow rate of 5 l min^{-1}. WELAS uses a high pressure Xenon arc lamp to illuminate a T-shaped mask which is imaged perpendicular to the particle beam into the measuring volume. A photomultiplier detects the light which is scattered into an angle of 90 ± 12°. Its field-of-view is bordered by another T-shaped mask, thereby defining a detection volume in the shape of two stacked cubes of different base areas. Pulse shape analysis is used to discriminate between particles P1 that pass entirely through the base area 280 × 280 $μm^2$ of the smaller cube, particles P2 that pass through the upper larger cube but not through the lower smaller cube, and other particles P3 that pass through the upper cube and along the border of the lower smaller cube. All particles P1 are counted, all particle counts P2 are rejected, while intermediate cases P3 are used for a correction. Thereby it is possible to measure particle size and number practically without border-zone-error. The instrument had been carefully calibrated in a preceding study (Benz et al., to be published) to accurately resolve cloud droplet diameters in the range 0.5–48 μm in 31 logarithmically spaced channels. It is important to note that the optical particle counter enables us to identify and count ice particles which are present in mixed cloud with reasonable accuracy. This is possible because homogeneously frozen cloud particles rapidly grow to much larger sizes than those of supercooled cloud droplets due to the Bergeron–Findeisen process. However, WELAS cannot size classify ice crystals perfectly because the *apparent* size of an ice crystal which is probed by the instrument is ambiguous: it depends on the accidental orientation of the crystals in the detection volume, in contrast to perfectly spherical cloud droplets. Therefore a significant but unknown fraction of the ice crystals cannot be detected under mixed cloud conditions because their *apparent* sizes remain below the ice detection threshold which

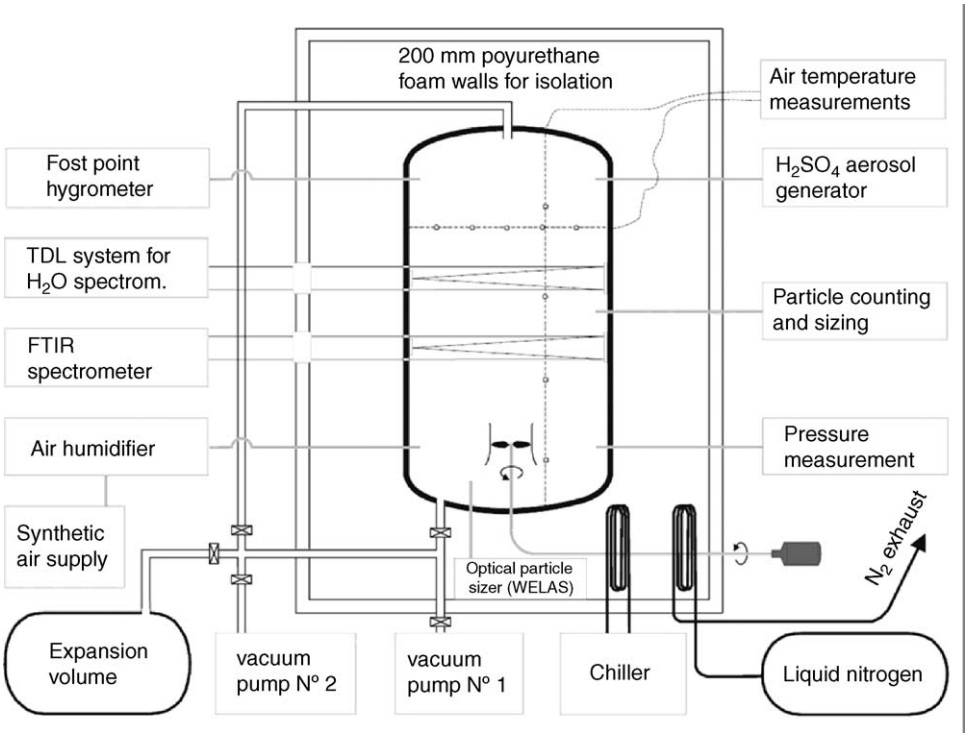

Fig. 1. Schematic view of the AIDA chamber in the thermostated containment. Only instruments used in this work are shown.

is set by the narrow size distribution of the supercooled cloud droplets. It is also not proven that all ice particles with apparent sizes exceeding the upper bound of 48 μm of the WELAS instrument are correctly attributed to the largest size bin.

Before starting the series of three experiments, the chamber was cooled to a temperature slightly below 0 °C, evacuated, and flushed several times with synthetic air. A predetermined amount of distilled water was then evaporated into the evacuated chamber which was subsequently brought to ambient pressure with particle-free synthetic air. The aluminium walls were internally coated with ice by slowly reducing the temperature over night to 243 K. On the following day sulphuric acid aerosol (median diameter at a concentration of 34 wt.% sulphuric acid: 200 nm, dispersion $\sigma = 2.3$) was admixed to the chamber as described elsewhere [24].

The number density of the sulphuric acid aerosol decreased by dilution from 360# cm^{-3} before the first experiment to 180# cm^{-3} before the last experiment. Note that these number densities are only a factor of two to three larger than in the clean upper troposphere [25,26], and can be significantly exceeded in some deep convective cloud systems, especially those forming over continents which can possess droplet number densities exceeding 800# cm^{-3} [14]. In spite of the ice-coated chamber walls the saturation ratio S_i with respect to ice remains less than unity under static conditions. This is due to a number of internal heat sources (ventilator, heated sampling lines and optical mirrors) which sustain a difference of up to 1.5 °C between the air temperature and the mean temperature of the ice-coated walls.

Two experiments were started at ~1000 hPa, and one at ~800 hPa, at a constant air temperature of approximately 243 K. To activate the sulphuric acid aerosol particles, the temperature was continuously lowered by operating the AIDA vessel as a moderate expansion chamber [24]. Expansion cooling was initiated by starting the mechanical pump(s), establishing exhaustion rates of 3 m^3 min^{-1} (experiment nos. 1 and 2) and 5 m^3 min^{-1} (experiment no. 3). Thereby the relative humidity was increased until the air became saturated with respect to liquid water, and a cold cloud was formed. The supercooled cloud droplets eventually started to freeze upon further cooling. Note that the cooling rate at constant pumping speed, Fig. 2, rapidly starts to deviate from the cooling rate of an adiabatically rising air parcel in the atmosphere which approximately obeys the adiabatic equation when latent heat release by condensation or freezing is negligible

$$\left(\frac{\mathrm{d}\ln T}{\mathrm{d}\ln p}\right)_{\text{adiabatic}} = \left(\frac{R}{c_\mathrm{p}}\right)_{\text{air}} \approx \frac{2}{7} \quad (1)$$

The deviation from (1) is mainly due to diabatic heating by the isothermal walls. The heat flux from the walls into the well-mixed chamber air is proportional to the temperature difference $\Delta T = T_{\text{wall}} - T_{\text{gas}}$ across a laminary boundary layer at the walls, mean thickness varying from several cm before to less than 1 cm during pumping. This diabatic heating effect sets a limit to the maximum ΔT which can be achieved in the AIDA chamber: effective cooling rates decrease continuously from initially 3 to 5 K min^{-1} immediately after starting one or both vacuum pumps, cf. Fig. 2, equivalent to 5–8 m s^{-1} updrafts in clear air.

We illustrate the experimental procedure by focussing on the time interval embracing the start of pumping, the formation of a supercooled water cloud, the freezing threshold marked by the first detection of ice particles with the optical particle counter, and the moment when the relative humidity starts to drop again

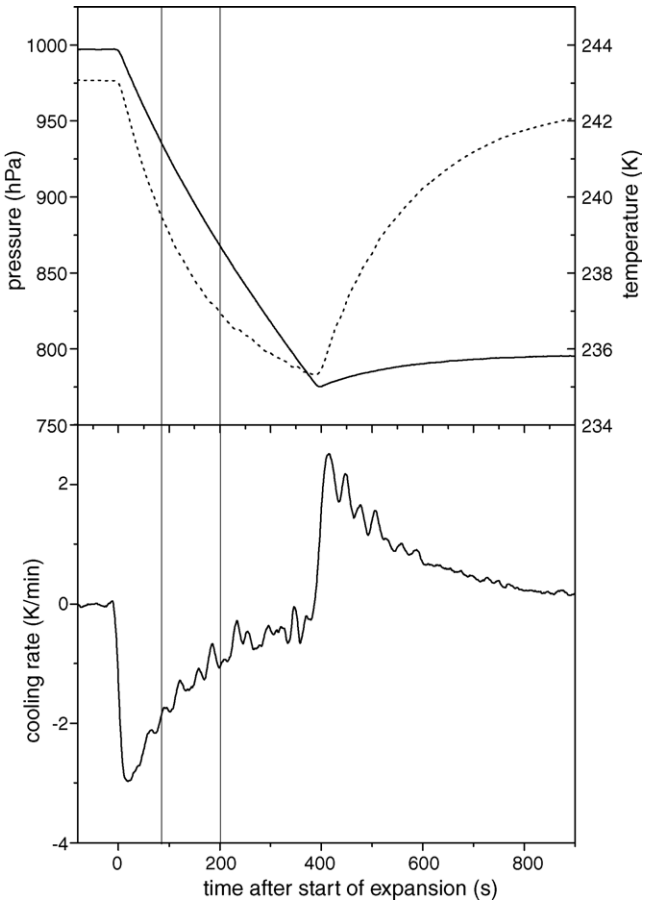

Fig. 2. Upper panel: pressure (solid line) and temperature (dashed line) profiles corresponding to an exhaustion rate of 3 m^3 min^{-1}. Vertical lines mark the formation of a supercooled liquid water cloud and the onset of homogeneous freezing, i.e. first detection of ice crystals by the optical particle counter. Lower panel: cooling rate (dT/dt) during and after the expansion.

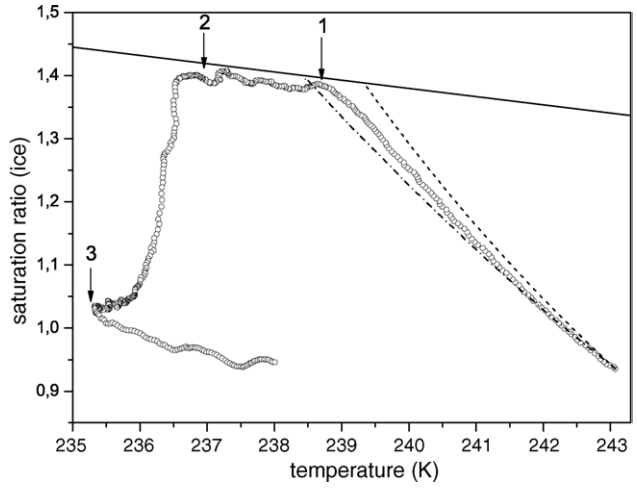

Fig. 3. Evolution of the saturation. Ratio S_i during an expansion experiment, starting with a sulphuric acid particle number density of 240# cm^{-3}. The significance of the dash-dotted and dashed lines are explained in the text. First arrow: formation of a supercooled water cloud; second arrow: onset of ice nucleation; third arrow: stop of pumping close to ice saturation at t = 400 s, cf. Fig. 4.

below 100% due to the Bergeron–Findeisen process. We also switch from time t, which is the independent variable in Fig. 2, to air temperature T as the new independent variable in Fig. 3 (note that both variables are related one-to-one in the time interval of interest via the temperature profile shown in Fig. 2). This has the advantage that we can calculate the variation of the saturation ratio S_i with respect to ice. The T-dependence of the saturation pressure over ice e_{si} is given to a very good approximation by the integrated approximate Clausius–Clapeyron equation [27]. A lower limit of S_i can be derived if we assume that the water vapour mixing ratio in the chamber air remains constant, neglecting the fact that the isothermal walls are internally coated with an ice film which can evaporate during the expansion process. In the absence of such a wall source the T-dependence of the saturation ratio $S_i(T)$ with respect to ice would be given by

$$S_i(T) = \frac{e(T_{start})}{e_{si}(T_{start})} \frac{p(T)}{p(T_{start})} \exp\left(+\frac{\Delta H_i}{R}\left(\frac{1}{T} - \frac{1}{T_{start}}\right)\right) \quad (2)$$

where e denotes water vapour pressure and p denotes total pressure. The enthalpy of sublimation, ΔH_i = 50.989 kJ mol^{-1}, was taken from the parameterisation of the vapour pressure $e_{si}(T)$ over ice by Marti and Mauersberger [28] who found that ΔH_i is constant between 170 and 250 K. However, since evaporation of ice from the isothermal chamber walls *does* occur and has the tendency to restore the partial pressure $e_{si}(T_{wall})$ in the chamber during expansions, the *true* partial pressure $e(T)$ in the chamber should be somewhat larger than the lower limit given by Eq. (2). An upper limit is obtained by setting $e(T) = e(T_{start})$ during expansions, i.e. assuming ultra-fast evaporation of water vapour from the ice-coated isothermal walls, maintaining a constant partial pressure throughout the chamber. In that case the factor $p(T)/p(T_{start})$ in Eq. (2) can be dropped. The actual time evolution of the saturation ratio S_i in the ice-coated chamber, circles in Fig. 3, lies between these two extremes, dash-dotted and dashed lines.

The solid line in Fig. 3 represents 100% relative humidity with respect to supercooled water. Here it is expressed in terms of the saturation ratio S_i with respect to ice, or more precisely in terms of the ratio between the saturation pressures over supercooled water and ice, e_{sw}/e_{si}, at the same temperature. Since both e_{sw} and e_{si} are not accurately known below about −20 °C [29] we have chosen to normalise the supercooled water line to the vapour pressure of ice using the following equation:

$$\frac{e_{sw}}{e_{si}} = \exp\left(-\frac{\Delta G_{freez}}{RT}\right) \quad (3)$$

where ΔG_{freez} is the free enthalpy of freezing. ΔG_{freez} has been derived by Speedy [30] from earlier measurements of molar heat capacities $c_p(T)$ of supercooled water which are in good agreement with more recent work [31,32].

When the ratio $S_i(T)$ measured with the TDL system reaches the water saturation line during an expansion cooling experiment (first arrow in Fig. 3), a supercooled water cloud is formed. The fact that the experimental data do not briefly overshoot the water saturation line (as predicted by model calculations, cf. Fig. 13a in [8]) but scatter systematically somewhat below the water saturation line is attributed to the combined uncertainties of the TDL

system, the vapour pressure over supercooled water [29], and the free enthalpy of freezing [30]. Cloud formation is confirmed by the optical particle counter which detects droplets with median diameters increasing rapidly from less than 1 μm to about 6 μm (mass median diameter about 8 μm). The first ice crystals are detected below a freezing threshold of about 237 K which is marked by the second arrow in Fig. 3. The growth of supercooled cloud droplets has also been retrieved from the FTIR spectra which confirm the onset of ice nucleation at about 237 K [22]. During the existence of large supercooled water droplets the experimentally determined saturation ratio $S_i(T)$ follows the water saturation line, Eq. (3), within the experimental uncertainty of the TDL system. This trend continues in the mixed cloud regime until cloud droplets are either frozen or have lost enough water by the Bergeron–Findeisen mechanism to become interstitial sulphuric acid particles again. A pure ice cloud with interstitial sulphuric acid aerosol particles has developed after the third arrow.

3. Results

It was the purpose of this work to retrieve homogeneous ice nucleation rates of supercooled water droplets from accurate time-resolved measurements of temperature, interstitial water vapour, supercooled cloud droplet number densities and size distributions, as well as ice particle number densities, in expansion cooling experiments. The cooling rates at the time of freezing varied between 0.7 K min^{-1} (experiment nos. 1 and 2) and 2.2 K min^{-1} (experiment no. 3), which corresponds to updrafts in clear air of 1.2 and 3.7 m s^{-1}, respectively. A typical record of the WELAS optical particle counter is shown in Fig. 4. Vertical bars enclose the time interval in which nucleation rates were analysed. The horizontal bar denotes the threshold above which particles are counted as ice crystals. The characteristic time needed by a just frozen medium-sized droplet to grow at 100% relative humidity to a size which exceeds the threshold for its identification as an ice particle amounted to about 7 s (experiment nos. 1 and 2), or 6 s (experiment no. 3) [33]. Note that in the experiment shown in Fig. 4 (upper panel) a small number of particles exceeded the threshold before freezing onset. These impurities, which were due to incomplete removal of seed particles from a preceding experiment, amounted to less than 2% of the final ice particle count and were therefore neglected.

Ice crystals which grow to large sizes by the Bergeron–Findeisen process may be lost by sedimentation. The magnitude of this loss was assessed by comparing the number densities of sulphuric acid particles before and after expansion cooling experiments: experiment no. 1 started with a number density of 360# cm^{-3}, which should drop to 288# cm^{-3} by dilution only. However, before the next expansion was started about 3.5 h later the particle number density was only 275# cm^{-3}. This sets an upper limit of 13 ice crystals cm^{-3} lost by sedimentation in experiment no. 1 if all other losses were negligible. Since the time interval during which nucleation rates were measured (vertical bars in Fig. 4) is short compared with the time during which ice crystals had time to grow and settle, we have made no corrections for sedimenting ice crystals.

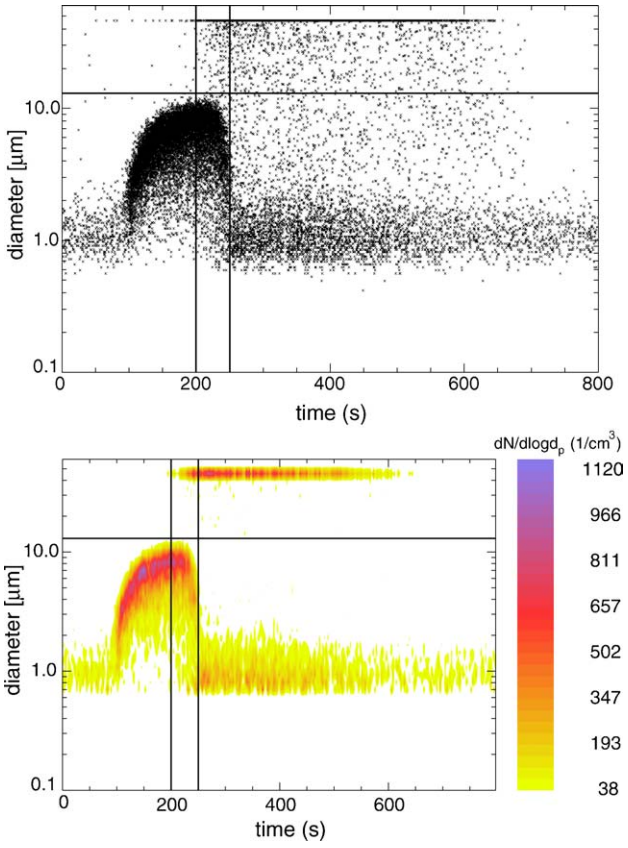

Fig. 4. Upper panel: original record of the WELAS optical particle sizer. Each dot marks a particle count in one of the 31 logarithmically spaced channels; note that ice particles with effective diameters exceeding 48 μm are attributed to the largest size bin. Lower panel: colour coded size distributions vs. experimental time. The vertical lines enclose the time interval in which nucleation rates were analysed.

Our measurements pertain to ice nucleation in dilute sulphuric acid droplets rather than in pure water, since the supercooled cloud was formed by activating sulphuric acid particles via expansion cooling. However, as can be seen in Fig. 5 the

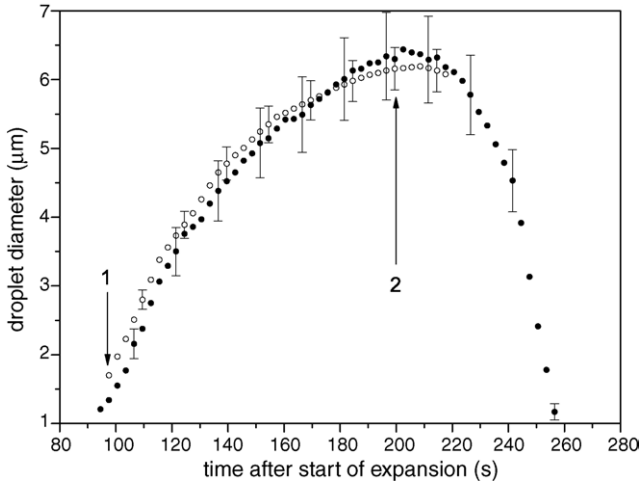

Fig. 5. Time evolution of cloud droplet number median diameters. Filled circles: determined with optical particle sizer WELAS; open symbols: diameters retrieved from FTIR spectra. Arrows have the same meaning as in Fig. 2.

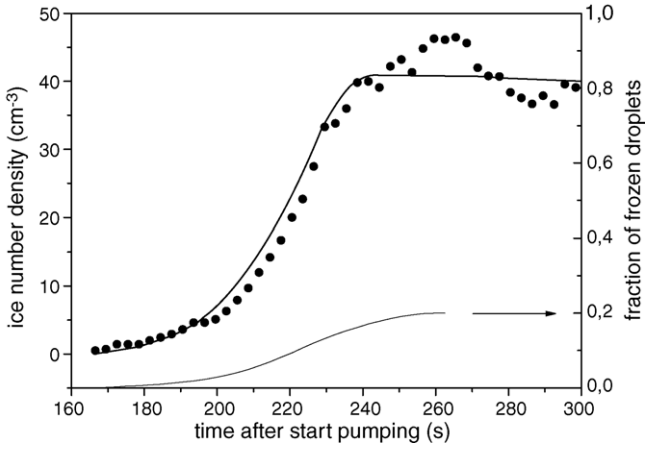

Fig. 6. Filled circles: number densities n_i of ice particles which were identified by the optical particle sizer WELAS during cloud freezing. Note that all data points were shifted 7 s to the left to account for the delayed detection of ice crystals by WELAS. Thick solid line: fit of the function (5) to the data points. Also shown is the fraction of frozen droplets, thin line, which increased to ca. 20% in this experiment.

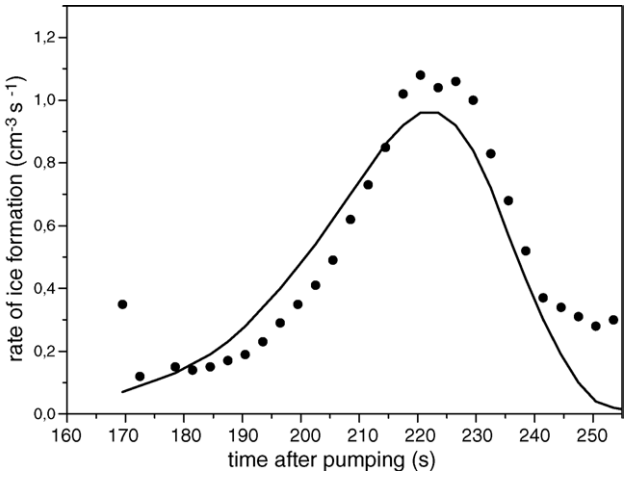

Fig. 7. Filled circles: derivative $(dn_i/dt)_t$ directly obtained from data points in Fig. 6, as explained in the text. Solid line: derivative $(dn_i/dt)_t$ of the fit function (5), represented by the solid line in Fig. 6.

freezing droplets were nearly two orders of magnitude larger than the sulphuric acid seed particles on which they were grown. A simple calculation shows that the sulphuric acid content of the supercooled cloud droplets was about 0.0015 wt.%, i.e. the water activity at the time of freezing was unity to a very good approximation. This issue will be resumed at the end of Section 4. Note the good agreement between droplet median diameters which were determined by two completely independent methods (sizing by the optical particle counter WELAS; analysis of FTIR spectra using Mie theory [22]), which lends credibility to the determined sizes and median volumes of the supercooled cloud droplets.

The following data analysis rests on the assumption that homogeneous ice nucleation is volume rather than surface-dominated. This is supported by recent results of Duft and Leisner [18], although these authors could not definitely exclude a notable contribution of surface nucleation to the homogeneous freezing of cloud droplets with diameters less than 8 μm which is about the mass median diameter of the freezing droplets in our experiments.

Fig. 6 focuses on the time interval between freezing threshold and the termination of significant droplet freezing which is due to the Bergeron–Findeisen process: the number density of ice particles $n_i(t)$ in the size range assigned to ice particles by the WELAS instrument first increases smoothly, then levels off at an ice particle number density which is about a factor of 2.5 less than the number density n_{liq} of the cloud droplets before freezing onset. The total number density $n_{tot} = n_i + n_{liq}$ (not shown) remains constant when corrected for dilution until the relative humidity drops below 100% (between arrows 2 and 3 in Fig. 3). Hereafter the increasing sub-saturation with respect to water causes the remaining cloud droplets to evaporate before they have a chance to freeze, which is the reason why only a small fraction of n_{tot} is converted to ice. The same phenomenon has been observed in homogeneously freezing clouds in the upper troposphere [25,26].

Nucleation rates $J(t)$ at each time step (or $J(T)$ at the corresponding temperatures) could be derived from the rates of new ice particle formation, the remaining number densities n_{liq} of cloud droplets, and their mass median volumes $v(t)$ using the following definition of the volume-dominated nucleation rate [19]:

$$J = \left(\frac{dn_i}{dt}\right)_t \frac{1}{v(t) n_{liq}} \quad (4)$$

Derivatives $(dn_i/dt)_t$ of the data $n_i(t)$ in Fig. 6 were obtained at each time step directly from the data points n_i using the data evaluation software IDL (Research Systems Inc., Boulder, CO, Version 6.1). This software fits a parabola to each set of three adjacent data points and calculates its derivative at the mid point. The obtained derivatives (filled circles) are shown in Fig. 7. These data are then combined with the known median volumes $v(t)$ and the number densities $n_{liq} = n_{tot} - n_i$ to calculate nucleation rates $J(T)$ for each time step.

The logarithms of the obtained nucleation rates, corrected for the known systematic errors (see below) are plotted versus the temperature in Fig. 8. Also shown are several parameterisations of the nucleation rate $J(T)$ as well as some experimental data from the literature, for comparison. For clarity we did not include the nucleation rate data of Krämer et al. [34] in the plot because they overlap our own data points, following very closely the parameterisation of Jeffery and Austin in the temperature range 236.1–237.3 K [13].

The results of this work are summarised in Table 1. We do not report the functions $J(T)$ because the temperature dependences of the measured nucleation rates, $(d \ln J/dT)$, are not sufficiently well defined in the narrow temperature range covered by our measurements, mainly because the ice crystal number densities n_i cannot be accurately determined in the presence of supercooled cloud droplets which have rotationally symmetric phase functions. This problem is underscored by the large and diverging vertical error bars in Fig. 8, which are discussed in Section 4. Another consequence of this problem is the fact

Table 1
Representative nucleation rates and fractional ice particle yields obtained in this work

Experiment no.	Cooling rate and total pressure at time of freezing	Evaluated temperature interval (K)	"Best" nucleation rates $\log J(T)$ (J in $\mathrm{cm^{-3}\,s^{-1}}$)	Fractional ice particle yields (%)
1	0.7 K $\mathrm{min^{-1}}$; 850 hPa	237.2–236.3	7.49 ± 0.28 at $T = 236.6$ K	18
2	0.7 K $\mathrm{min^{-1}}$; 850 hPa	237.2–236.4	7.27 ± 0.25 at $T = 236.7$ K	20
3	2.3 K $\mathrm{min^{-1}}$; 690 hPa	237.5–236.1	8.16 ± 0.24 at $T = 236.6$ K	68

The uncertainty ranges of the $\log J$ data include known systematic errors, but exclude uncertainties of T_{gas} and $\nu(t)$, see the discussion in Section 4. Note that the pumps were started at 1000 hPa in experiment nos. 1 and 2, but at 800 hPa in experiment no. 3.

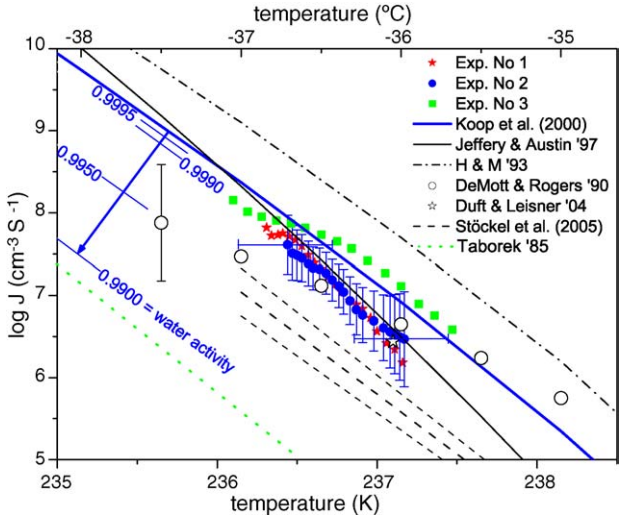

Fig. 8. Filled symbols: nucleation rates $J(T)$, this work, including corrections for all *known* systematic uncertainties, error bars shown for one experiment only. Thick solid line: parameterisation of the nucleation rate by Pruppacher [10] and adopted by Koop et al. [35] in their parameterisation of $J(T,a)$, as explained in text; thin solid line: parameterisation proposed by Jeffery and Austin [13]; dash-dotted line: parameterisation based on measurements in clouds by Heymsfield and Miloshevich (H & M) [26]; large open circles: cloud chamber study by DeMott and Rogers [19]; dashed line with error range (thin dashed lines): levitated droplet measurements by Stöckel et al. [36]; open star: levitated droplet measurement by Duft and Leisner [18]. Short dashed line in lower left corner: emulsified droplet measurements of Taborek [37].

that experiments no. 1 and 2 with similar exhaustion rates of 3 $\mathrm{m^3\,min^{-1}}$ yield similar nucleation rates $J(T)$, while experiment no. 3 with an exhaustion rate of 5 $\mathrm{m^3\,min^{-1}}$ yields a significantly larger nucleation rate and a different temperature dependence which nearly coincides with the parameterisation of Pruppacher [10]. Table 1 lists "representative" nucleation rates $J(T)$, one for each experiment. They are reported for those temperatures where the corresponding error bars (Fig. 8) are minimal. We also report fractional ice particle yields, defined as the number of ice particles formed per number of droplets available at freezing onset, which depend on the cooling rate at the time of freezing.

4. Discussion of systematic and random errors

A very important but *unknown* systematic error results from the temperature measurements which are fundamental to all nucleation rate determinations, irrespective of the experimental method. We estimate that the calibration error of our gas temperature sensors does not exceed ±0.3 K. This range, which is the same for all data from the AIDA chamber experiments, is shown by the horizontal error bars in Fig. 8. Due to the strong temperature dependence of the nucleation rate this error alone makes the obtained nucleation rates $J(T)$ uncertain by a factor of 3 in both directions. Another systematic error arises from the delayed detection of newly frozen ice particles with the optical particle sizer. As outlined in the first paragraph of Section 3, it takes about 7 s until a just frozen droplet can be identified as an ice particle by the WELAS instrument. This systematic error was accounted for by shifting all data in Fig. 8 systematically to warmer temperatures by 0.08 K for experiment nos. 1 and 2, and by 0.23 K for experiment no. 3, although this *increases* the discrepancy between the nucleation rates obtained at low and high cooling rates.

We argue that the nucleation rate derived from experiment no. 3 should be given less weight in comparison with experiment nos. 1 and 2, for the following reasons:

- All measurements of T_{gas} are routinely corrected for the time constant of the temperature sensors, approximately 3 s. The correction is usually small, but becomes substantial for the large cooling rate in experiment no. 3, which may have caused an error of a few tenths of a Kelvin.
- In experiment nos. 1 and 2 the mass median diameters of the freezing droplets changed slowly and thus could be easily tracked by the optical particle counter during the main icing phase of about 60 s. This phase was compressed to only 20 s in experiment no. 3, and the mass median diameter changed from 9 to less than 2 μm within 10 s.

Small timing errors of the rapidly changing mass median diameters result in large uncertainties of $\nu(t)$, which translate into large uncertainties of the nucleation rate $J(T)$ via Eq. (4).

A subtle systematic error which affects all experiments equally arises from random fluctuations of the air temperature during expansion cooling events. These fluctuations are due to turbulent mixing, driven by updrafts close to the chamber walls which act as a heat sources, and subsidence in the centre where the air would cool adiabatically in the absence of turbulent mixing. Fig. 9 shows typical temperature fluctuations which were measured with an ultra fast NTC thermistor during an expansion event, about 1 m away from the chamber walls. By weighting the frequency of occurrence of the amplitudes ΔT with the nucleation rate $J(T)$ we have derived a "weighted mean gas temperature" which is 0.05 K colder than the measured mean gas temperature. This small correction is also included in the results shown in Fig. 8.

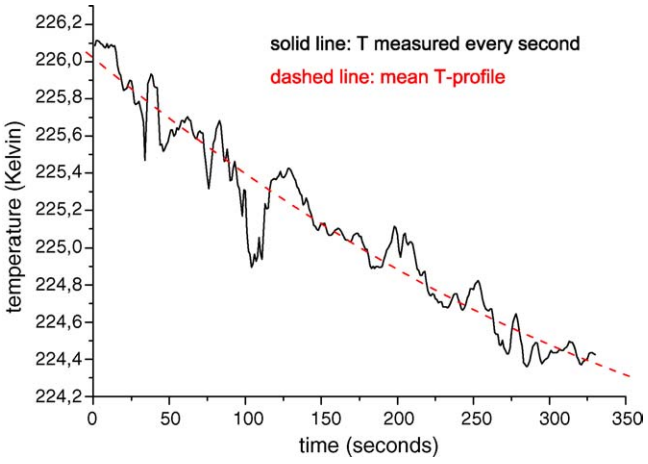

Fig. 9. Temperature fluctuations during an expansion cooling experiment measured with an ultra fast temperature sensor.

The vertical error bars in Fig. 8 (only shown for experiment no. 2 for clarity) represent overall statistical uncertainties of the dynamic rate measurements. They were estimated as follows: in a first step we fit a smooth function $P(t) \times n_{\mathrm{tot}}$ through the data points $n_i(t)$ in Fig. 6, as described in the next paragraph. The derivative of this function yields the bell-shaped solid line in Fig. 7. In a second step we evaluate the deviations of the individual data points from the bell-shaped curve. These deviations are then used to estimate relative uncertainties of the experimentally determined derivatives $(\mathrm{d}n_i/\mathrm{d}t)_t$. The combination of these uncertainties with the statistical uncertainties of the median volumes $v(t)$ and number densities n_{liq} of the liquid droplets via Eq. (4) yields the vertical error bars in Fig. 8.

The function fitted to our data points in Fig. 7 was constrained by considering the probability $P(t)$ that n_i droplets out of a total number $n_{\mathrm{tot}} = n_i + n_{\mathrm{liq}}$ of particles have frozen until time t. This probability is given by

$$P(t) = \left(\frac{n_{\mathrm{ice}}}{n_{\mathrm{tot}}}\right)_t = 1 - \exp\left(-\int_{t_0}^{t} v(t)[J(t)\,\mathrm{d}t]\right)$$
$$= 1 - \exp\left(-\int_{T_0}^{T} \frac{1}{\gamma} v(T) b [J(T)]^c\,\mathrm{d}T\right) \quad (5)$$

Integration starts at time $t_0 = 0$, temperature T_0 above freezing threshold; $v(t)$ is the time-dependent median volume of the supercooled droplets which is obtained from the WELAS measurements, and $\gamma = (\mathrm{d}T/\mathrm{d}t)_t$ is the (smoothed) cooling rate taken from the lower panel in Fig. 2. The factor b and the exponent c are introduced as fitting parameters. The fit starts with the parameterisation $J(T)$ of Pruppacher [10]. Note that $\log J(T)$ is approximately a linear function of the temperature in the range covered by our measurements. Variations of b and c in Eq. (5) result in vertical displacements of the straight line and change the slope of the line. The parameters b and c were varied until the experimental data in Fig. 6 were reasonably well fitted. The not perfect fit of Eq. (5) may be due to the inability of the WELAS instrument to properly count non-spherical ice particles, as discussed in the experimental part. We have therefore optimised the fit parameters b and c in Eq. (5) individually for each measurement. The derivative of the fit function yields the bell-shaped curve, solid line in Fig. 7, which was needed to construct the error bars in Fig. 8.

We now resume the issue of the sulphuric acid content on the nucleation rate measurements. Koop et al. have measured critical ice nucleation temperatures of aqueous sulphuric acid droplets over a wide range of concentrations [38]. An extrapolation of their results to pure water was in excellent agreement with Pruppacher's parameterisation of $J(T)$ [10]. In a more recent paper Koop et al. presented evidence that this parameterisation can be generalised to include nucleation rates of aqueous solution droplets with known water activities a [35]. We have used the generalised parameterisation to calculate $J(T,a)$ for water activities of 0.9995, 0.9990, 0.9950, and 0.9900. Short sections of the corresponding functions $J(T,a)$ are shown in the upper left corner of Fig. 8. Note that the water activity of the droplets studied in this work was a >0.9999 at freezing onset and did not drop below 0.998 before the freezing rate became negligible due to the decreasing number and volume $v(t)$ of unfrozen droplets. Taking the activity dependence of the nucleation rate into account resulted in a very small correction. This confirms our earlier conclusion that the sulphuric acid content did not affect our nucleation rate measurements.

5. Comparison with literature data

We focus on ice nucleation in natural clouds which plays an important role in deep convective systems and contributes to cirrus formation. Freezing of cloud drops occurs in a narrow temperature window, approximately between −35 and −38 °C [8]. Fig. 8 compares our results with other literature data and parameterisations in this range. At significantly lower temperatures freezing of haze droplets occurs in the atmosphere before cloud droplets can form at water saturation. Nucleation rates of pure water below about −40 °C are therefore mainly of theoretical interest and will not be discussed here.

Largely different techniques have been used in the past to measure ice nucleation rates in water drops. Since our main interest is in atmospheric applications we will first address cloud chamber experiments which simulate atmospheric conditions. The first experiments in a larger cloud chamber (μm-sized cloud drops, updrafts of ∼2.5 m s^{-1}) were reported by DeMott and Rogers [19]. Their methodology was similar to ours, except that they simulated true adiabatic expansion cooling rates with the help of a temperature programmed perforated cold shield which enclosed a controlled volume of 1.2 m^3. However, their measurements of ice particle number densities as function of temperature required a significant settling time correction, in contrast to our actively sampling optical particle counter. The results of DeMott and Rogers are represented by large open circles in Fig. 8. The authors assigned temperature independent error bars (shown only once in Fig. 8) to their nucleation rates [19]. These are in excellent agreement with our data at 236.6 K (−36.5 °C) where our results are most reliable, and in reasonable agreement within the temperature range of our study, although the temperature dependences diverge.

Freezing rate measurements of water drops levitated in a temperature controlled Paul trap, pioneered by Baumgärtel, Wöste and coworkers [39], were reported in a series of papers [18,34–36,39,40]. The most recent results, represented by the thick dashed line in Fig. 8 (thinner dashed lines indicating the error range), fall about an order of magnitude short of our measurements [36]. An earlier study had yielded somewhat higher rates [34] (not shown in Fig. 8 because they practically coincide with our experiment nos. 1 and 2). The authors also investigated the effect of droplet charging and found no influence on the nucleation rate. An important result has already been mentioned in Section 3: Duft and Leisner could show that the nucleation rate exactly scales with the droplet volume, thereby excluding a significant contribution of surface nucleation, at least for diameters larger than 8 μm [18]. Their data point, open star in Fig. 8, agrees with our measurements. It is a significant advantage of the technique that the volume of a levitated droplet can be accurately determined using Mie theory. Less reliable is the determination of the droplet temperature which rapidly equilibrates with the gas temperature. This is only accurately known when the temperature of the complicated trap body is perfectly uniform.

Nucleation rates have also been measured successfully using water-in-oil emulsions. It is a drawback of the technique in the context of this paper that it does not simulate environmental conditions. Most importantly, the drops must be stabilised with a surfactant which can give rise to surface-induced ice nucleation. We have selected the data of Taborek [37] because these authors have carefully assessed this problem: they could show for one particular detergent that the nucleation rate scaled *exactly* with the volume of 6 and 300 μm droplets. These data are represented by the dotted line in the left-lower corner of Fig. 8. It remains an open question why they fall more than two orders of magnitude short of most other nucleation rates. However, the data are very accurate in terms of their temperature dependence, and this agrees well with most other studies including our data.

Nucleation rate expressions $J(T)$ have also been compared with field measurements. Heymsfield and Miloshevich [26] used a microphysical model to interpret aircraft measurements in cold lenticular wave clouds. They adopted a special parameterisation of $J(T)$ which was available at the time, and which is represented by the dash-dotted line in Fig. 8. They found that "the homogeneous ice nucleation rates from the measurements are consistent with the temperature-dependent rates employed by the model (within a factor of 10^2, corresponding to about 1 °C in temperature) in the temperature range −35 to −38 °C". The same model was used very recently to interpret aircraft data from the CRYSTAL-FACE campaign [8]. However, the above-mentioned special parameterisation was replaced by the generalised parameterisation $J(T,a)$ of Koop et al. [35] which is represented by the thick line in Fig. 8 for pure water drops ($a = 1$).

6. Conclusions

The nucleation rates obtained in this work were measured under simulated atmospheric conditions, and should therefore be directly comparable with the results of DeMott and Rogers [19] who performed a similar study. The agreement between both studies is indeed excellent at 236.6 K where our own measurements are most reliable, and probably theirs as well. Equally good agreement was found with most of the single levitated droplet studies which cover a similar temperature range, with the exception of the most recent study by Stöckel et al. [36] who report about an order of magnitude lower nucleation rates. All studies except one [19] yield similar temperature dependences which more or less parallel the T-dependence of the generalised parameterisation proposed by Koop et al. [35]. We therefore suggest that the rate data of DeMott and Rogers [19] and our own data at 236.6 K should be adopted in atmospheric modelling studies, but combined with the temperature dependence of the generalised parameterisation of Koop et al. [35]. The T-dependence is supported by a large variety of experiments, including our own work and a study of droplet freezing in emulsions which was particularly suited to determine temperature dependences [37]. To be on the safe side, we extend the uncertainty ranges quoted in Table 1 by including the estimated systematic error of our gas temperature measurements which introduces an uncertainty by a factor of three, as outlined in Section 4. This yields the following recommended values:

- $\log J(236.6\,\mathrm{K}) = 7.5 \pm 0.8$;
- $\log J(236.7\,\mathrm{K}) = 7.25 \pm 0.75$;
- $\log J(236.6\,\mathrm{K}) = 8.2 \pm 0.75$.

The last value is the least reliable, as discussed in Section 4.

To resolve the issue of the correct temperature dependence, larger numbers and more accurate nucleation rate measurements should be performed under simulated atmospheric conditions, and over a wider temperature range. Furthermore, the transition from cloud droplet to haze particle freezing [35] should also be probed, extending and improving our earlier AIDA chamber measurements of critical ice nucleation temperatures which were performed with sulphuric acid aerosols well below 235 K [24]. It has also been suggested recently that we measure nucleation rates for a wider size range of cloud drops in the AIDA chamber, in order to distinguish between surface and volume-induced ice nucleation [41]. This would require larger variations of the seed particle number densities to extend the measurements to smaller-sized supercooled droplets. Whether these issues could be successfully addressed depends mainly on instrumental improvements. An essential development concerns correct and highly time-resolved measurements of ice particle number densities, n_i, in the presence of supersaturated droplets. More trivial but at least equally important are very accurate, precise, and fast measurements of the gas temperature and its fluctuations.

We consider the successful determination of homogeneous ice nucleation rates in simulated supercooled clouds as a proof-of-concept, demonstrating the suitability of the AIDA chamber at the Forschungszentrum Karlsruhe to study cloud microphysical processes quantitatively.

Acknowledgements

We are indebted to the technical crew of IMK-AAF for their competent support of these and all other experimental investigations at the AIDA chamber facility. This work contributes to the Virtual Institute "Zentrum Tropische Tropopause – ZTT" which is supported by the Presidential Funds of the Helmholtz Gemeinschaft Deutscher Forschungszentren. Helpful suggestions of an anonymous reviewer are much appreciated.

References

[1] N.J. Bunce, J.S. Nakai, M. Yawching, J. Photochem. Photobiol. A 57 (1991) 429–439.
[2] IPCC, Intergovernmental Panel on Climate Change, in: J.T. Houghton, et al. (Eds.), Climate Change: The Scientific Basis, Cambridge University Press, New York, 2001.
[3] J. Crawford, R.E. Shetter, B. Lefer, C. Cantrell, W. Junkermann, S. Madronich, J. Calvert, J. Geophys. Res. 108 (D16) (2003) 8545, doi: 10.1029/2002JD002731.
[4] B.L. Lefer, R.E. Shetter, S.R. Hall, J.H. Crawford, J.R. Olson, J. Geophys. Res. 108 (D21) (2003) 8821, doi: 10.1029/2002JD003171.
[5] A. Eliassen, D. Blanchard, T. Bergeron, Bull. Am. Meteorol. Soc. 59 (1978) 387–392.
[6] G. Vali, J. Aerosol. Sci. 16 (1985) 575–576.
[7] B. Kärcher, U. Lohmann, J. Geophys. Res. 107 (D23) (2002) 4698.
[8] A.J. Heymsfield, L.M. Miloshevich, C. Schmitt, A. Bansemer, C. Twohy, M.R. Poellot, A. Fridlind, H. Gerber, J. Atmos. Sci. 62 (2005) 41–64.
[9] K. Sassen, in: K.D. Lynch, et al. (Eds.), Cirrus, Oxford University Press, 2002, pp. 11–40.
[10] H.R. Pruppacher, J. Atmos. Sci. 52 (1995) 1924–1933.
[11] Th. Koop, Z. Phys. Chem. 218 (2004) 1231–1258.
[12] J. Huang, L.S. Bartell, J. Phys. Chem. 99 (1995) 3924–3931.
[13] C.A. Jeffery, P.H. Austin, J. Geophys. Res. 102 (D21) (1997) 25269–25279.
[14] D. Rosenfeld, W.L. Woodley, Nature 405 (2000) 440–442.
[15] M. Matsumoto, Sh. Saito, I. Ohmine, Nature 416 (2002) 409–413.
[16] A. Tabazadeh, Y.S. Djikaev, H. Reiss, Proc. Natl. Acad. Sci. 99 (25) (2002) 15873–15878.
[17] Y.G. Chushak, L.S. Bartell, J. Phys. Chem. B 103 (1999) 11196–11204.
[18] D. Duft, T. Leisner, Atmos. Chem. Phys. 4 (2004) 1997–2000.
[19] P.J. DeMott, D.C. Rogers, J. Atmos. Sci. 47 (1990) 1056–1064.
[20] O. Möhler, S. Büttner, C. Linke, M. Schnaiter, H. Saathoff, O. Stetzer, R. Wagner, M. Krämer, A. Mangold, V. Ebert, U. Schurath, J. Geophys. Res. 110 (2005) D11210, doi: 10.1029/2004JD005169.
[21] V. Ebert, H. Teichert, C. Giesemann, H. Saathoff, U. Schurath, Tech. Messen 72 (2005) 23–30.
[22] R. Wagner, St. Benz, O. Möhler, H. Saathoff, M. Schnaiter, U. Schurath, J. Phys. Chem. (2005), ASAP Article, doi: 10.1021/jp051942z.
[23] M. Seifert, R. Tiede, M. Schnaiter, C. Linke, O. Möhler, U. Schurath, J. Ström, J. Aerosol Sci. 35 (2004) 981–993.
[24] O. Möhler, O. Stetzer, S. Schaefers, C. Linke, M. Schnaiter, R. Tiede, H. Saathoff, M. Krämer, A. Mangold, P. Budz, P. Zink, J. Schreiner, K. Mauersberger, W. Haag, B. Kärcher, U. Schurath, Atmos. Chem. Phys. 3 (2003) 211–223.
[25] K. Sassen, G.C. Dodd, J. Atmos. Sci. 45 (1988) 1357–1369.
[26] A.J. Heymsfield, L.M. Miloshevich, J. Atmos. Sci. 50 (1993) 2335–2353.
[27] P.W. Atkins, Physical Chemistry, 5th ed., Oxford University Press, Oxford, 1994.
[28] J. Marti, K. Mauersberger, Geophys. Res. Lett. 20 (1993) 363–366.
[29] D.M. Murphy, T. Koop, Q. J. R. Meteorol. Soc. 131 (2005) 1539–1565.
[30] R.J. Speedy, J. Phys. Chem. 91 (1987) 3354–3358.
[31] E. Tombari, C. Ferrari, G. Solvetti, Chem. Phys. Lett. 300 (1999) 749–751.
[32] D.G. Archer, R.W. Carter, J. Phys. Chem. B 104 (2000) 8563–8584.
[33] H.R. Pruppacher, J.D. Klett, Microphysics of Clouds and Precipitation, 2nd ed., Kluwer Academic Publishers, Dordrecht, The Netherlands, 1997.
[34] B. Krämer, O. Hübner, H. Vortisch, L. Wöste, T. Leisner, M. Schwell, E. Rühl, H. Baumgärtel, J. Chem. Phys. 111 (1999) 6521–6527.
[35] Th. Koop, Beiping Luo, A. Tsias, Th. Peter, Nature 406 (2000) 611–614.
[36] P. Stöckel, I.M. Weidinger, H. Baumgärtel, Th. Leisner, J. Phys. Chem. A 109 (2005) 2540–2546.
[37] P. Taborek, Phys. Rev. B 32 (1985) 5902–5906.
[38] Th. Koop, H.P. Ng, L.T. Molina, M.J. Molina, J. Phys. Chem. A 102 (1998) 8924–8931.
[39] M. Krämer, M. Schwell, O. Hübner, H. Vortisch, T. Leisner, E. Rühl, H. Baumgärtel, L. Wöste, Ber. Bunsenges. Phys. Chem. 100 (1996) 1911–1914.
[40] P. Stöckel, H. Vortisch, T. Leisner, H. Baumgärtel, J. Mol. Liq. 96/97 (2002) 153–175.
[41] J.E. Kay, V. Tsemekhman, B. Larson, M. Baker, B. Swanson, Atmos. Chem. Phys. 3 (2003) 1439–1443.